Nonlinear feedback control of bi-modality in the wake of a three-dimensional bluff body

D. Ahmed[*] and A. S. Morgans[†]

Department of Mechanical Engineering,
Imperial College London, London, SW7 2AZ, UK.

(Dated: June 30, 2022)

The turbulent wake behind a square-back Ahmed body in close proximity to the ground exhibits bi-modal switching. This manifests as the centre of the wake switching between one of two asymmetric positions, either horizontally or vertically. Switches occur over random timescales, with the wake recovering symmetry in the long time-average. The present work employs wall-resolved large eddy simulations to investigate feedback control for suppressing horizontal (lateral) wake bi-modality of a square-back Ahmed body at $Re_H \sim 3.3 \times 10^4$ based on the body height. Base-mounted pressure sensors are used to estimate the position of the wake as an input signal for the controller, while actuation targets the near-wake region via synthetic jets emanating from a gap around the perimeter of the Ahmed body base. A nonlinear feedback controller based on a Langevin model of the wake dynamics is synthesized. This successfully suppresses the wake lateral bi-modal switching. However, this switching is replaced by a time-periodic streamwise motion of the large coherent structure occupying the near-wake region, leading to amplification of the higher frequency dynamical wake modes. The action of feedback control also leads to base pressure recovery and a reduction in pressure drag. Upon varying the controller parameters, a trade-off between the degree of bi-modality suppression and drag reduction is observed. A maximum drag reduction of 7.4% is achieved for a semi-symmetrised wake, with a fully symmetrised wake achieving 2.5% reduction. Bi-modality suppression is proposed to have an indirect link to drag reduction through the effect of the wake state on the separated free shear layers and the upstream boundary layers.

I. INTRODUCTION

The relevance of bluff bodies to the transportation industry drives the need for bluff body aerodynamic drag reduction. Ground vehicles such as lorries, buses and light-duty vehicles are classified as bluff bodies. Sudin *et al.* [1] indicated that the aerodynamic drag consumes 50% of the total fuel burnt by a passenger car at typical highway speeds, compared to 65% for trucks, as reported by Seifert *et al.* [2]. The drag force exerted on a solid body moving in a fluid stream is classified into pressure drag and friction drag [3]. The former is related to the pressure difference between the frontal and rear sections of the body in the streamwise direction, while the latter is associated with the friction between the surfaces of the solid body and the moving fluid, i.e. the development of boundary layers. For bluff bodies, pressure drag (also known as form drag) dominates, constituting approximately 80% of the total drag in case of flow past an Ahmed body [4].

The pressure drag of a bluff body largely arises due to the pressure deficit on the rear part of the body caused by large-scale flow separation. It depends on the location of flow separation as well as the dynamics and topology of the wake flow downstream of the body. For three-dimensional bluff bodies whose flow separation position is fixed, including axisymmetric [5, 6] and rectilin-

ear [4, 7, 8] bluff bodies, some key common dynamical features can be identified. These include the development of boundary layers along the body surfaces, which separate at the rear edges of the body, creating free shear layers which bound the recirculation region in the near wake. The recirculation region extends from the rear part of the body up to the so-called free stagnation point. The shear layers experience Kelvin-Helmholtz instability, thus amplifying disturbances in the wake downstream of the body. The interaction between each parallel pair of separated shear layers leads to coherent vortex shedding in the wake [9]. The whole recirculation region also exhibits a pumping motion in the streamwise direction, which is associated with oscillations of the free stagnation point in the wake [7]. Instabilities related to symmetry breaking are also observed in the wake of 3D bluff bodies, which will be discussed in further detail.

The present study considers a three-dimensional blunt bluff body in the form of the square-back Ahmed body, representing a simplified road vehicle geometry. The time-averaged wake topology and characteristic frequencies of the square-back Ahmed body were the focus of early studies by Ahmed *et al.* [4] and Mason and Beebe [10] and are now well-established. A further unsteady wake behaviour has recently been identified [11, 12], known as bi-modality, or bi-stability. It manifests as random switching of the wake between off-centred (asymmetric) preferred positions. While the time-averaged turbulent wake exhibits symmetry, instantaneously the wake exhibits a random switching between two asymmetric states, with the timescales between switching events being relatively long. Similar wake symmetry-breaking

_____

[*] d.ahmed18@imperial.ac.uk; Department of Mechanical Engineering, Imperial College London, London, SW7 2AZ, UK.
[†] a.morgans@imperial.ac.uk

behaviour has been observed in the wakes of other bluff bodies. The laminar flow past a sphere at sufficiently high Reynolds number exhibits axisymmetry breaking in the wake, which increases the drag, the degree of increase increasing with Reynolds number [13]. The laminar wakes of blunt-based axisymmetric bodies similarly transition from axisymmetry to a planar symmetry as Reynolds number increases past a critical value. For turbulent wake conditions, this rotational symmetry breaking is preserved, with a random dynamical behaviour in the azimuthal position of the symmetry plane [5] – this is known as multi-modality or multi-stability. A similar behaviour is observed in the turbulent wake of the sphere [6]. Compared to axisymmetric bodies, the symmetry of the base surface of the square-back Ahmed body, permits only two azimuthal positions of the wake, promoting bi-modality instead of multi-modality.

The wake of a square-back Ahmed body evolves according to a similar symmetry pattern to that for axisymmetric bodies. In the laminar flow regime, Reflectional Symmetry Breaking (RSB), first occurs when the Reynolds number exceeds a critical value. This value has been experimentally found to be 365 (based on body height) for the square-back Ahmed body with a ground proximity of 60% of the body height [12]. The steady symmetric state of the wake transitions to steady asymmetric after a short unsteadiness period. The wake maintains this asymmetric state at higher Re numbers in the laminar flow regime. As Reynolds number increases, an unsteady bifurcation emerges, causing periodic vortex shedding in the wake. The same laminar flow sequence of RSB was captured numerically by Evstafyeva et al. [14]. In the turbulent regime, the RSB static modes arising from the laminar flow bifurcations have been shown to persist. However, turbulent perturbations now cause the wake to switch randomly between off-centred preferred positions [15]. The wake resides at one stable asymmetric position until it is sufficiently perturbed to be able to switch to the other reflected position. This behaviour is found to be Re-independent in the turbulent flow regime up to a value of at least Re of 3×10^6, matching the scale of real road vehicles in driving conditions [16]. The associated topology shift is the skewness of the near wake toroidal-vortex towards and away from the base surface [11, 17, 18]. The instantaneous asymmetric position of the wake is correlated with the proximity of one of the sides of the toroidal-vortex structure to the base.

Bi-modality or random reflectional symmetry breaking (RSB) in the wake has been the subject of several recent experimental studies [11, 12, 16, 19–23]. It is a uni-directional behaviour that occurs either in the horizontal (side-to-side) or vertical (top-to-bottom) direction, depending on the aspect ratio of the body base, the ground proximity and the yaw angle. Grandemange et al. [16] mapped the direction of the bi-modality, for a $0°$ yaw angle, as a function of the base aspect ratio and the ground clearance. Three regimes were identified, depending on the ground clearance normalized by the body width, C^*. For low ground clearances, $C^* < 0.05$, horizontal switching occurs for $0.3 < H/W < 0.65$, where H and W are the base height and width respectively. For slighter larger ground clearances, $0.05 < C^* < 0.09$, wake switching is inhibited, as a result of the detachment of the under-body flow. For $C^* > 0.09$, bi-modal switching occurs in the direction of the longest edge. Plumejeau et al. [23] recently investigated the effect of the under-body flow on the interactions of the wake dynamics, noting that the transition of the wake to bi-modal was accompanied by a change in the frequency of the vortex shedding mode. Barros et al. [24] investigated the sensitivity of the wake dynamics to disturbances induced in the under-body flow, introducing a coupling based on Langevin dynamics between the vertical wake asymmetry and the horizontal bi-modality.

In terms of numerical investigations, Rao et al. [25] captured the asymmetry of the turbulent wake past the Ahmed body, using the unsteady partially-averaged Navier-Stokes (PANS) simulations. Eddy-resolving techniques employing Large Eddy Simulations (LES) and Detached Eddy Simulations (DES) captured the spatial symmetry breaking of the wake but not the switching [26–29]. Dalla Longa et al. [18] was the first numerical study which captured the bi-modal switching behaviour of the wake behind three dimensional blunt bluff bodies; a square-back Ahmed body and a lorry model. The study employed wall-resolved LES to simulate the flow. It suggested that wake switching events are associated with a stochastic shedding of a hair pin vortex in the near wake region. The LES study by Hesse and Morgans [30] further suggested that the upstream separation bubble just aft of the body nose is generates disturbances linked to the wake switching. The direct numerical simulation (DNS) results by Podvin et al. [31] captured the deviation of the wake and indicated the same dynamics shown in the LES results except bi-modality.

Wake bi-modality has been found to have implications for drag. The experimental study by Grandemange et al. [11] found that wake bi-modality contributes up to 9% to pressure drag and creates unfavourable side forces and moments that affect the stability of the body. Haffner et al. [22] showed that the averaged base pressure coefficient reduced by 9% during the switching events of the wake compared to the asymmetric wake. The wake is instantaneously symmetric during these switching events, indicating that wake re-symmetrisation has a favourable effect on the base pressure and consequently the pressure drag. The sensitivity of the friction drag to bi-modality suppression has not as yet been investigated, to the authors' knowledge, with most previous studies presuming that the wake state affects the drag via base pressure recovery.

The effect of wake re-symmetrisation on drag has been exploited in passive and active flow control studies. In terms of passive control, Evrard et al. [32] used a base cavity to suppress wake bi-modal switching, achieving a 9% drag reduction, while Grandemange et al. [33] posi-

tioned a vertical cylinder in the center of the recirculation region, preserving wake symmetry and reducing drag by 5%. Active flow control studies which target wake symmetrisation have so far achieved much smaller drag reductions than the above passive control approaches. This may be due to the restriction of forcing with body-mounted actuators, as Grandemange et al. [33] suggested that the most receptive region for actuating the wake is the center of the recirculation region. The experimental study by Brackston et al. [21] used linear feedback control to re-symmetrise a turbulent wake, reducing the drag by around 2%. An opposition control strategy was experimentally applied by Li et al. [34] to symmetrise the wake; feedback control based on harmonic forcing successfully symmetrised the wake, but promoted lateral vortex shedding, limiting the drag reduction to be only slight. Schmidt et al. [35] showed that active control could suppress both bi-modality and higher frequency dynamics, but the bubble pumping mode persisted. In most cases, the use of linear feedback control to suppress bi-modality was found to significantly augment wake fluctuations around the center, as compared to the original fluctuations around the uncontrolled asymmetric position. Additionally, forcing the flow in the near-wake region enhances turbulent activity in the free shear layers, promoting high-frequency dynamics in the wake and also inhibiting drag reduction.

In this paper, we investigate the potential of a non-linear single-output (SISO) feedback control approach for suppressing the side-to-side wake bi-modal switching. To the authors' knowledge, this is the first attempt at applying a nonlinear control approach to the three-dimensional wake of a squareback Ahmed body. High fidelity, wall-resolved LES are used to simulate the dynamics of the turbulent wake, to implement the nonlinear feedback control and to investigate the effect of the controller on the wake bi-modality, the wake dynamics more generally and the drag. The feedback control set-up employs base pressure sensing and synthetic jet actuation through a small gap around the perimeter of the base. The controller is based upon a reduced order model employing the Langevin equation, adapted for a rectilinear geometry. This model, developed by Rigas et al. [15] for an axisymmetric body, and adapted for rectilinear bodies by Brackston et al. [21], accurately captures the evolution of wake reflectional symmetry breaking and random bi-modal switching. The paper discusses the simulation setup in section §II, the wake dynamics of the unforced case in section §III. Section §IV provides the details of the model for wake bi-modality. The design methodology of the nonlinear feedback controller is provided in section §V. The effect of the feedback control on the bi-modality, drag and wake dynamics is presented in section §VI. A sensitivity study of the controller non-linearity on bi-modality suppression and the flow properties is further investigated in section §VII. Finally, a comparison of the flow field between the unforced and the controlled cases is preformed using modal reduction (proper orthogonal
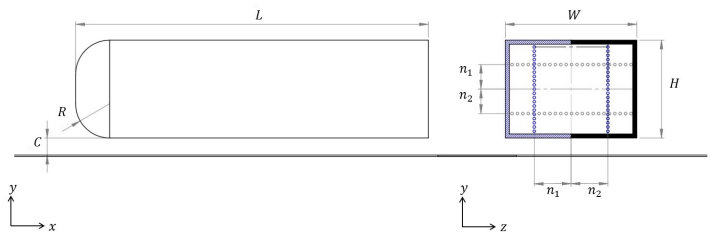

FIG. 1: Ahmed body scaled by one fourth, with height $H = 72mm$. The circles on the base show the sensor positions used to calculate the vertical (grey) and horizontal (blue) pressure gradients. Actuation is via synthetic jets placed around the base perimeter with a thickness of $0.04H$; actuation is antisymmetric in z as shown by the blue dashed and the black solid areas.

decomposition) and is shown in §VIII.

II. SIMULATION SETUP

Wall-resolved Large Eddy Simulation (LES) is used to simulate the turbulent wake downstream of a square-back Ahmed body and as a test-bed for the non-linear feedback control approach. The dimensions of the square-back Ahmed body are similar to those used by Ahmed et al. [4], scaled by one quarter, as shown in figure 1. The aspect ratio of the body cross-section is W/H=1.35, where W and H are the body width and height, respectively. The length of the body is $L^* = L/H = 3.63$. The clearance between the bottom surface of the body and the ground is $C^* = C/H = 0.174$. The frontal part is rounded with a radius of $R^* = R/H = 0.35$. The Reynolds number based on the body height is $_H = 3.3 \times 10^4$. The solution domain is $(L_{inlet}, L_x, L_y, L_z) = (2L, 8L, 2L, 2L)$, where L_{inlet}, L_x, L_y and L_z are the domain length upstream of the body, the total domain length in the streamwise direction, the transverse domain length and the domain length in the spanwise direction respectively, as shown in figure 2. The blockage factor, defined as the ratio of the Ahmed body cross-section to the domain cross-section, is 2.5%, small enough to neglect confinement effects. The size of the domain has been chosen according to ERCOFTAC recommendations [36, 37].

The inflow used is a steady uniform velocity profile corresponding to the value of Re_H. A no-slip boundary condition is used on the ground and the body surfaces, with a free-slip condition set on the domain sides. A convective outlet condition is set on the domain outlet to avoid backflow. The OpenFOAM CFD toolbox (version 6.0 [38]), employing a finite volume formulation, was used for the simulations. The governing incompressible Navier-Stokes equations are solved using the PIMPLE algorithm, which is a hybrid algorithm of the Pressure Implicit with Splitting of Operators (PISO) and Semi-Implicit Method for Pressure-Linked Equations (SIM-

PLE) algorithms. The LES employs the Wall-Adapting Local Eddy-viscosity (WALE) model to account for turbulence at sub-grid scales [39]. Second order spatial and temporal discretisation schemes were employed.

Unstructured hexahedral cells were used employing the trimmer cells model in StarCCM+ software. This creates hexahedral cells in the solution domain, trimming the mesh core at the boundaries to form polyhedral cells. The prism layers model was used near the solid surfaces to create orthogonal cells, resolving the near-wall flow, as indicated in figures 3 and 4. Three different computational grids of 9, 11 and 15 million cells were considered. The refinement criteria were based on minimising the cell sizes in the prism layers, the refined region around the body and the far field region. The mesh near the wall, in the prism layers, is refined to fully resolve the boundary layer for each of the three computational grids, maximising the surface region over which $\overline{y^+} \leq 1$, as shown in figure 5 for the case of 11×10^6 cells. The normalised near-wall grid sizes in the streamwise and spanwise directions are $\overline{x^+} \leq 39$ and $\overline{z^+} \leq 40$, respectively, following the mesh requirement for LES [40]. A growth rate of 1.1 is used between the different mesh zones, as shown in figures 3 and 4, to minimize the computational cost [30].

For each of the three computational grids, the values of the body drag coefficient, $\overline{C_D}$, the average base pressure, $\overline{C_{\text{PBase}}}$, and the normalised length of the recirculation region, $\frac{\overline{L_R}}{H}$, were calculated and compared to the experiments of Grandemange *et al.* [16], conducted at $Re_H \sim 3.3 \times 10^4$, and the numerical study of Hesse and Morgans [30]. The maximum deviation from the experimental values for the length of the recirculation region and the average base-pressure were about 2% and 15%, respectively. For the latter, it is noted that the deviation from the experimental results of Fan *et al.* [41] is just 4%, suggesting that experimental values for the base pressure span a range. All three values are comparable to the simulation results of Hesse and Morgans [30]. Based on these comparisons and the values of y^+_{max} shown in Table I, the mid-size computational grid with 11 million cells is selected for the simulations. The value of $y^+_{\text{Max}} \leq 1$, confirming that the near wall regions are fully-resolved. We further note that the average cell size in the wake region resolves the Taylor microscale, which represents the minimum turbulent length scale to be resolved by the LES [42].

Having validated the LES approach for accurately simulating the wake flow, we now describe the adaptations to the simulations needed in order to implement feedback control. The feedback control set-up employs base pressure sensing and synthetic jet actuation through a small gap around the perimeter of the base, as shown in figure 1. For the actuation, a time-dependent boundary condition is needed (only) at the location of the actuator slots. The actuation signal, given by the controller output value, must be calculated at each timestep in response to the time-varying input sensor signal from the pressure probes. This is implemented using the

Mesh size ($\times 10^6$ cells)	$\overline{C_D}$	$\overline{C_{\text{PBase}}}$	$\frac{\overline{L_R}}{H}$	$\overline{y^+}$	y^+_{Max}
15	0.362	-0.22	1.43	0.10	0.6
11	0.360	-0.22	1.42	0.58	1.0
9	0.352	-0.20	1.45	0.95	3.0
Exp. [16]	-	-0.19	1.41	-	-
Sim. [30]	0.364	-0.20	1.42	-	< 1

TABLE I: Mesh Independence study, based on the time-averaged drag ($\overline{C_D}$), time-averaged base pressure ($\overline{C_{\text{Pbase}}}$), time-averaged recirculation length ($\overline{L_R}$), time-averaged and maximum y^+

$SWAK4FOAM$ (SWiss Army Knife for OpenFOAM) library [43]. $SWAK4FOAM$ is a plugin $C++$ library, which allows the use of a user-defined time-varying equation to prescribe the values at the boundary, instead of the default constant value in OpenFOAM.

The drag and pressure coefficients used in analysing the data in the following sections are calculated as shown in equations (1) and (2) respectively. $D(t)$, ρ and U_∞ represent the drag force, air density and free stream velocity respectively. $P(x, y, z, t)$ represents the pressure at a position (x, y, z) in space at an instant t and P_∞ is the free stream pressure. The spatial gradient of the pressure coefficient in direction n is calculated as shown in equation (3), where n represents a cross-flow direction (y, z). n_1 and n_2 are the distances between the base pressure probes (either side of the base centre line) and the center of the base in the direction n, M is the number of the probes and N is the total length of the base in the same direction, as shown in figure 1.

$$C_D(t) = \frac{D(t)}{\frac{1}{2}HW\rho U_\infty^2} \tag{1}$$

$$C_P(x, y, z, t) = \frac{P(x, y, z, t) - P_\infty}{\frac{1}{2}\rho U_\infty^2} \tag{2}$$

$$\frac{dC_P(t)}{dn} = \frac{\sum_M C_P(n_1, t) - \sum_M C_P(n_2, t)}{\frac{M(n_1+n_2)}{N}} \tag{3}$$

The momentum coefficient C_μ is defined as the ratio of momentum imposed through the actuators to the free stream momentum and is given by equation 4. Equation 5 is used to calculate the actuation power $Pw_{actuation}$, where $\overline{U_{\text{jet}}}$ and η_{actuator} represent the time-averaged jet velocity and the efficiency of the actuator, respectively. The total power saved due to drag reduction, Pw_{saved}, is calculated as shown in equation 6, where ΔF_{drag} is the change in the drag force.

$$C_\mu(t) = \frac{A_{\text{actuator}}\overline{U_{\text{jet}}^2}}{A_{\text{base}}U_\infty^2}, \; A_{\text{actuator}} = W_{\text{actuator}}H, \; A_{\text{base}} = WH \tag{4}$$
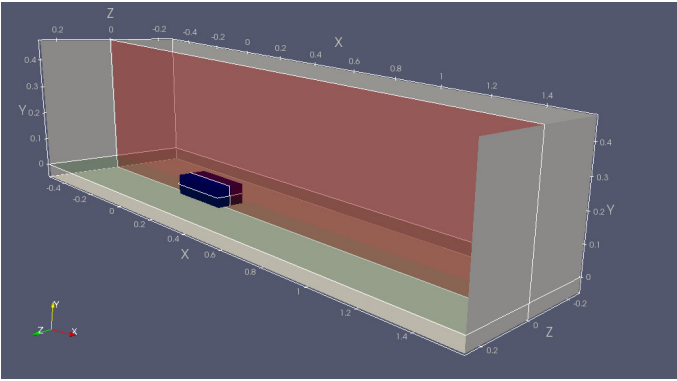
FIG. 2: Solution domain with a vertical body-centred plane (red) and horizontal body-centred plane (green). Point $(0, 0, 0)$ is located on the base center.
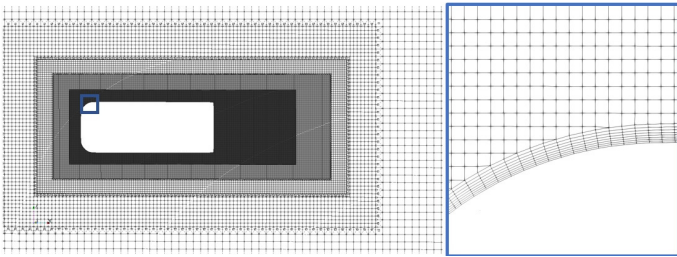

FIG. 3: Mesh details on the vertical plane (xy). The zoomed view (in the blue box) shows the prism layers on the body surface.

$$Pw_{\text{actuation}} = \frac{A_{\text{actuator}}}{\eta_{\text{actuator}}} \frac{\rho \overline{U_{\text{jet}}^3}}{2} \qquad (5)$$

$$Pw_{\text{saved}} = \Delta F_{\text{drag}} U_\infty \qquad (6)$$

III. UNFORCED FLOW

The spatial gradients of the pressure coefficient on the base of the Ahmed body are used to characterise wake bimodality. Figure 6 depicts the instantaneous gradient of
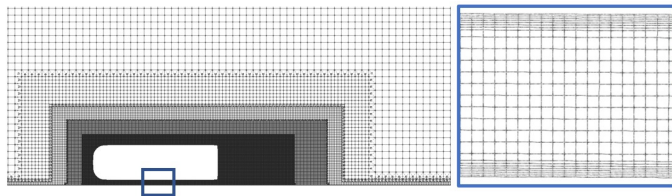

FIG. 4: Mesh details on the horizontal plane (xz). The zoomed view (in the blue box) shows the prism layers used to resolve the boundary layers on both the body and the ground surfaces.
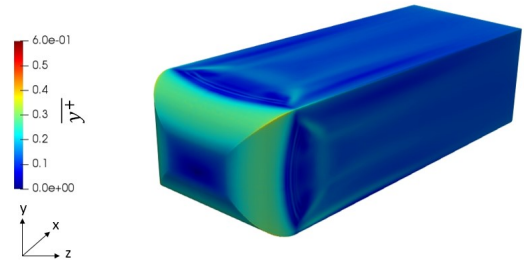

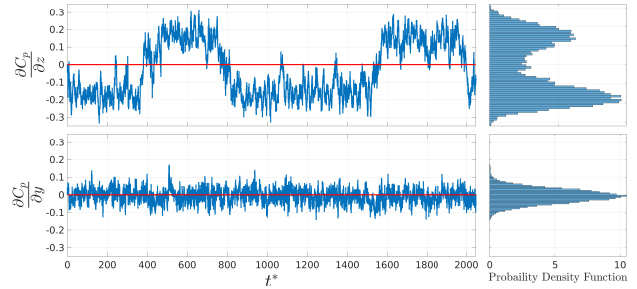FIG. 5: $\overline{y^+}$ distribution on the Ahmed body.

FIG. 6: Time evolution of the horizontal (top) and vertical (bottom) gradients of pressure coefficient on the base.

the pressure coefficient in the horizontal (spanwise) and vertical (transverse) directions, denoted as $\partial C_p / \partial z$ and $\partial C_p / \partial y$, respectively, where z and y are normalised by W and H, respectively. The dimensionless time t^* is defined as $t^* = (tU_\infty)/H$. The wake exhibits horizontal bi-modal switching in a random manner, with the simulation over 2000 convective time units capturing four switches of the wake. The wake is approximately symmetric in the vertical direction, its slight asymmetry caused by the jet generated by the underbody flow. The most probable asymmetric positions of the wake correspond to a horizontal gradient of pressure coefficient of ± 0.20, similar to the values obtained numerically for the same Re_H but using a different code [18]. The maximum time maintained by the wake in one asymmetric position is 750 normalised time units, with an average switch duration being 25 normalised time units. The time-averaged drag coefficient is 0.36, which matches values reported in the literature [29, 30, 44]. The length of the recirculation bubble is $L_R = 1.42H$, defined based on the time-averaged streamwise velocity, and the time-averaged pressure coefficient $\overline{C_{\text{Pbase}}} = -0.22$, consistent with the experimental results of Grandemange *et al.* [16] and the LES results of Hesse and Morgans [30]. The time-averaged pressure coefficient during the switching, when the wake is instantaneously symmetric, is -0.21 compared to -0.232 for the asymmetric wake states.

A vortex ring structure, toroidal in shape, is formed in the near wake region, matching previous studies
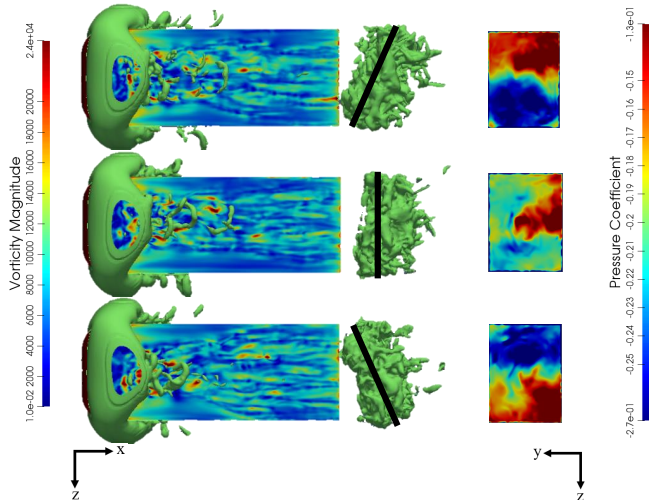
FIG. 7: Left: Iso-contours of the coefficient of pressure $C_P = -0.2$, as well as the vorticity distribution on the body top surface, indicating the near wake vortical structures for different wake positions. Right: The associated C_p on the base.

[8, 9, 20, 45–47]. Horizontal bi-modal switching causes the near wake toroidal structure to tilt towards and away from the base stochastically. During the switching period, the toroidal structure becomes instantaneously parallel to the base, representing a symmetric wake. This effect is projected onto the base pressure as a low-pressure region associated with the vortical structure being locally close to the base. Figure 7 shows this behaviour and the associated base pressure for the three cases, when the wake is tilted towards the positive z direction, during switching when the wake is instantaneously symmetric and after the switching when it is tilted towards the negative z direction. These results are consistent with previous experimental [12] and numerical results [18] which capture side-to-side bi-modality.

IV. BI-MODALITY MODEL

The present work adopts a nonlinear feedback control approach in order to target suppression of the bi-modal switching, which is itself a non-linear phenomenon. The controller will be based upon a stochastic model in the form of a nonlinear Langevin equation, which captures the evolution of the reflectional symmetry breaking in the turbulent wake of the Ahmed body. This model was initially developed to characterise the random symmetry breaking behaviour in the turbulent wake of an axisymmetric body, this exhibiting multi-modal behaviour [15]. It is based on the premise that multi-modality occurs due to the persistence of the laminar global modes at high Reynolds number, with the turbulent fluctuations acting to push stochastically between asymmetric stable posi-

tions. The deterministic part (the drift) of the Langevin model captures the nonlinear dynamics of the reflectional symmetry breaking in the laminar flow regime, employing the typical Landau equation. The stochastic part represents the effect of turbulent fluctuations.

$$r(t)t = -\lambda r^3 + \alpha r + \sigma \zeta(t) \tag{7}$$

Brackston et al. [21] adapted the model for rectilinear bodies exhibiting bi-modality, such as the squareback Ahmed body. Barros et al. [24] employed a coupled Langevin model to represent the transition of the wake form the vertical asymmetric state to a horizontal bi-modal with vertical symmetry. The adapted Langevin model is shown in equation (7). The parameter r is some measure of the modal amplitude, α is the growth rate and λ the saturation parameter. The first two terms on the right hand side represent the spatial symmetry breaking mode, which arises due to a supercritical pitchfork bifurcation at laminar Reynolds numbers, as described in Section I. The last term represents the turbulent broadband forcing acting on the coherent structures of this mode, with $\zeta(t)$ a random dynamics of a standard Wiener process and σ^2 the noise intensity; it is expected to capture all flow disturbances that cause wake switching between the two asymmetric states.

The parameter chosen to characterise the wake mode position, $r(t)$, is the centre of pressure on the base, calculated as shown in equation (8), where $P(x,y,z,t)$ is the pressure and W the width of the base and A_{base} is the base area. A value of $r(t) = 0$ corresponds to a symmetric wake. According to the model, $r(t)$, moves within closed bounds around one of the two asymmetric states until sufficiently perturbed by the stochastic term to switch to the other. The corresponding probability density function of $r(t)$, obtained experimentally at different Re, shows little dependence on Re in the turbulent regime [21].

$$r(t) = \frac{1}{W \iint_{A_{base}} P(x,y,z,t)\,dA} \iint_{A_{base}} zP(x,y,z,t)\,dA \tag{8}$$

The model parameters for the current Ahmed body, $(\alpha,\lambda,\sigma^2)$, were identified by fitting the model to the unforced flow data. The time-averaged mean square displacement (MSD) of the centre of pressure, $r(t)$, is shown in figure 8a. Its value is calculated as $\langle (r(t+\delta t)-r(t))^2 \rangle$, where δt here has the same value as the simulation timestep. The findings are consistent with those of Rigas et al. [15]: the MSD is found to be proportional to the lag time, δt, before starting to plateau. A linear least square fit was used to estimate the value of the noise intensity for the short time scale region, where $\langle (\Delta r(\delta t))^2 \rangle = 2\sigma^2 \times \delta t$. The value of the noise intensity is found to be $\sigma^2 = 0.64$. The probability density function (PDF) of the model, obtained using the steady-state Fokker Plank equation (equation (9), where C represents a normalising constant), was matched to the probability density function
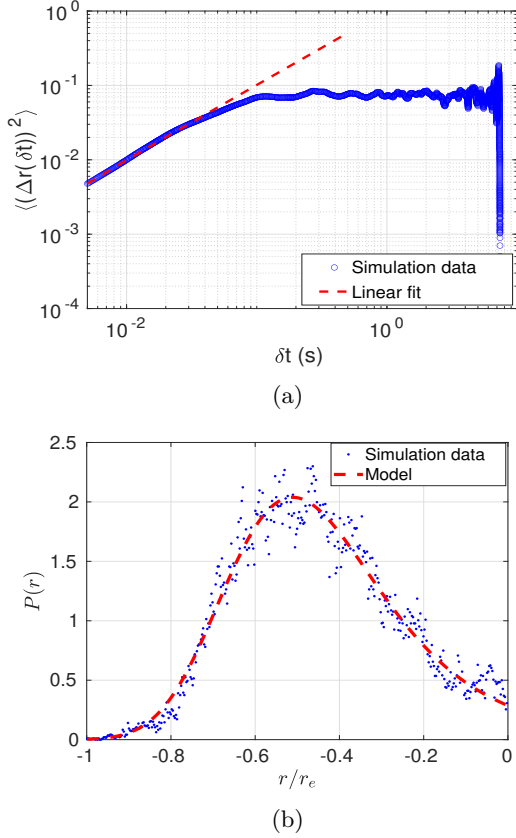
(a)

(b)

FIG. 8: (a) Mean Square Displacement (MSD) of the centre of pressure $r(t)$ in the unforced case (blue) and a linear fit (red dashed line) to estimate the noise intensity σ^2. (b) Probability Density Function of the model (dashed red line) and the data of one asymmetric stable position of the wake (blue dots).

of $r(t)$ from the unforced simulation (figure 8b). This allowed estimates of both α and λ to be obtained as *3.6* and *91.0* respectively. With reference to Barros *et al.* [24], the values of these parameters are for a weakly vertically asymmetric wake, as identified for the unforced case.

$$P(r) = C \exp\left(\frac{\alpha}{\sigma^2} r^2 - \frac{1}{2}\frac{\lambda}{\sigma^2} r^4\right) \qquad (9)$$

V. FEEDBACK CONTROL DESIGN

Due to the strongly non-linear behaviour underpinning the bi-modal switching [15], we seek to develop a nonlinear feedback controller based upon the above Langevin model. The sensor signal, $r(t)$, which acts as the input signal to the controller, is a measure of the horizontal centre of pressure on the base. $r(t)$ is calculated by placing 48 sensors on the base of the Ahmed body at a horizontal normalised distance of $\Delta z = 0.125$ between each

successive sensors and a vertical normalised distance of $\Delta y = 0.17$. The output signal from the controller is then fed to the synthetic jet actuators, which are located in a gap around the outer perimeter of the base with a width of $0.04H$. The jet actuation is purely in the streamwise i.e. x-direction. It is horizontally antisymmetric, such that the actuation on the right is in anti-phase with the actuation on the left as shown in figure 1. At any instant in time, the actuation has zero-net-mass-flux, since the left and right mass injection cancels: streamwise momentum is sucked from one side of the base and blown through the other. Thus a single signal dictates the spatial variation around the whole actuation perimeter. The block diagram of the single-input single-output feedback control is shown in figure 9.

Based on this system, a Lyapunov function based nonlinear controller was synthesized. The application of this technique for controlling nonlinear systems was introduced by Artstein [48], who established a link between the continuous stabilisation of a nonlinear system and the existence of a control Lyapunov function. In this study, a quadratic Lyapunov function is used, as defined through equation (10). $V(r)$ is a positive definite function which is continuously differentiable and decreases with time, i.e. $V(r) > 0, \forall \mid r \mid > 0$ and $V(0) = 0$. The negative definite derivative of the Lyapunov function, shown in equation (11), guarantees the asymptotic stability of the closed-loop controlled system for the given range of r that corresponds to the position of the asymmetric wake in the unforced case [49]. The control law is represented by equation (12), where $u(r)$ is the controller signal sent to the actuator, A and B are time-independent amplification factors and λ and α are the model parameters estimated from the unforced case results in section IV. The controller signal $u(r)$ represents the non-dimensional actuator jet velocity, i.e. $u(r) = U_{jet}(t)/U_\infty$. The robustness of the controlled system to variations in the controller parameters was was examined. The controller was found to be asymptotically stable for $0 < (\alpha, \lambda) \leq \infty$. The amplification parameter B, must be a positive value to maintain the asymptotic stability of the controlled system. A represents a scaling parameter of the controlled signal.

$$V(r) = \frac{1}{2} r^2 \qquad (10)$$

$$\frac{dV}{dt} = \frac{dV}{dr} \times (\dot{r} + u(r)) , \dot{V} < 0 , \dot{V}(0) = 0 , \forall \mid r \mid > 0 \qquad (11)$$

$$u(r) = -A(-\lambda r^3 + (B+\alpha)r) \qquad (12)$$

This feedback control algorithm was implemented in the LES using the *SWAK4FOAM* (SWiss Army Knife for Foam) library for OpenFoam [43]. The value of the center of pressure, r, is calculated in real time at the relevant simulation timestep and fed to the controller. The
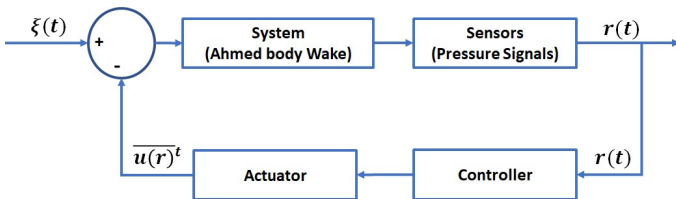
FIG. 9: Block diagram of the feedback control loop.

FIG. 10: Horizontal (top) and vertical (bottom) gradients of the coefficient of pressure C_P (left) before and after switching the controller on (black dashed line). The corresponding Probability Density Functions, PDF (right) for the uncontrolled case (blue bars) and the controlled case (orange line). the controller parameters A and B are 10 and 60, respectively.

inherent nonlinearities of the flow necessitate a response time of the wake flow. This is accounted for by employing the weighted moving average of $u(r)$, denoted $\overline{u(r)}^t$ and shown in equation (13) where β is a weighting coefficient given by the ratio of the simulation timestep (Δt) to a characteristic time equivalent to $St_H \sim 2$, taken to be the maximum frequency resolved in the unforced flow. Applying the weighted moving average limits the unsteadiness introduced to the streamwise momentum in the wake, which contributes to the drag [50].

$$\overline{u(r)}^t = \beta u(r)^t + (1-\beta)\overline{u(r)}^{t-\Delta t} \qquad (13)$$

VI. FEEDBACK CONTROL IMPLEMENTATION

The feedback controller is implemented in simulations, initially with controller parameters $A = 10$ and $B = 60$. The simulation shown in figure 10 initially has control switched off, during which time the wake switches once in the horizontal direction. The controller is switched on at $t^* = 640$, with the convective time for the controlled duration of the simulation being 1230. This is significantly greater than the maximum residence time of the wake in a given asymmetric state the unforced case ($t^* = 750$) and is thus deemed statistically sufficient for investigating the controller performance. The effect of the feedback controller are explored in the following subsections, assessing first its effect on the main control objective – suppressing the wake bi-modal switching – as well as its effect on the mean flow properties, the mean body drag and the other dynamical wake modes.

A. Bi-modality suppression

The main control objective is to suppress the stochastic switching of the wake, as characterised by the horizontal base pressure gradient. The effect of the controller on both the horizontal and vertical pressure gradients is shown in figure 10. It is evident that the wake switching behaviour in the horizontal direction is completely suppressed. The probability density function of the horizontal base pressure gradient ($\partial C_P/\partial z$) exhibits just a single peak around the center in the presence of control.
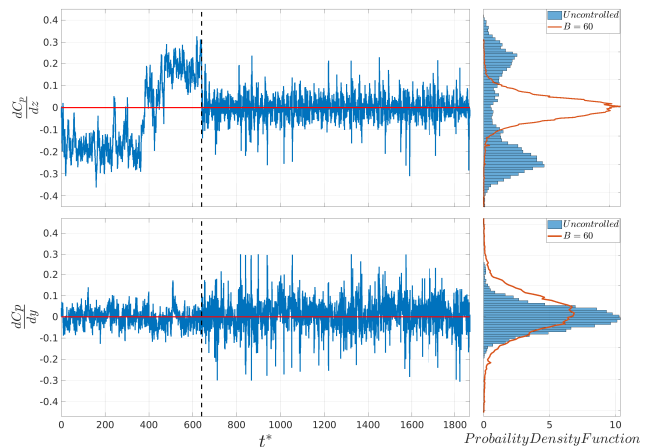
Although the controller was designed to target the deterministic part of the bi-modality model – the static RSB modes – as discussed in section IV, it also affects the wake oscillations around the main wake position. These oscillations, which we will term "residual oscillations", are caused by the turbulent disturbances modelled via the stochastic term in the absence of control in equation (7). A reduction in the level of these residual oscillations – in the horizontal direction – is achieved after switching the controller on. Thus an advantage of the nonlinear controller is that it results in much reduced maximum horizontal wake offset positions. In the presence of control, the maximum offset wake position corresponds to a horizontal pressure gradient of $\sim \pm 0.08$, which is a 72% reduction in the uncontrolled value of ± 0.29. This is partly due to the wake symmetrisation and partly due to the reduced amplitude of the residual oscillations.

Thus, the effect of the controller extends beyond reorienting the asymmetric wake to also alter the higher frequency wake dynamics. These residual oscillations are linked to interactions between the lateral shear layers and the asymmetric wake, consistent with the switching mechanism recently proposed by Haffner *et al.* [22], and may also be partially related to the disturbances convected from the upstream boundary layer dynamics. The degree of reduction in the residual oscillations depends on the ratio between the non-linear and linear terms of the control law, as it will further be discussed in section VII. The amplitude of the residual oscillations value can be quantified by the root-mean-square of the trajectory of r_{RMS} at any main position of the wake (equation 14, where N is the number of data points of the controlled

convective time). The feedback controller reduces the amplitude of the horizontal residual oscillations by up to 20% compared to the unforced case. The wake then exhibits regular time-periodic behaviour with a distinguishable frequency, St_{control}. Similar time periodic behaviour has been observed after implementation of other control strategies, as in case of the opposition control by Li *et al.* [34] and the adaptive control by Varon *et al.* [51]. It is notable that the residual wake oscillations are not only reduced compared to the unforced case, they are also much smaller than has been observed so far after application of linear controllers [21, 34]. For the latter, the amplitude of residual oscillations of the symmetrised wake matched the original asymmetric extremes of the wake, two orders of magnitude larger than for the unforced flow. This suggests that the underpinning non-linear dynamics of the wake, when neglected, amplify the wake residual oscillations in the bi-modality direction.

In the orthogonal (vertical) direction, the controller is observed to have a negligible effect on the mean wake position, but to slightly amplify the vertical residual oscillations, as shown in figure 10 ($\partial C_P / \partial y$).

$$r_{\text{RMS}} = \left[\frac{1}{N} \sum_{i=0}^{N} r_i{}^2 \right]^{1/2} \tag{14}$$

B. Mean flow properties and wake topology

This section will explore the effect of the controller on the mean flow properties and the near wake toroidal-vortex structure, for which stochastic bi-modal switching resulted in tilt variations for the unforced case. The effect of control is to orientate this toroidal structure parallel to the base, so that it is approximately horizontally symmetric, as shown in figure 11. This matches the instantaneous orientation of the wake during a switching event for the unforced case (figure 7), with the symmetric state being unstable in the absence of control. The resulting base pressure coefficient exhibits a higher pressure region near the centre of the base surrounded by a region of lower pressure, as shown in figure 11. The base pressure coefficient here differs to the unforced case of figure 7, where it has minima and maxima on the sides of the base for the asymmetric wake, and looks similar to the instantaneous unstable symmetric wake. The time-averaged base pressure coefficient of the controlled wake is $\overline{C_{\text{Pbase}}} = -0.227$, which represents $\sim 2\%$ reduction in the base pressure compared to the asymmetric wake. This value depends on the amplification parameter, B, in the control law (equation 12), which will further be discussed in section VII.

The effect of the controller suggests that exchanging momentum within the wake region directly effects the streamwise position of the toroidal-vortex. Comparing the topology of the symmetrised wake to that when a base-cavity is used [32], for the latter drag reduction was
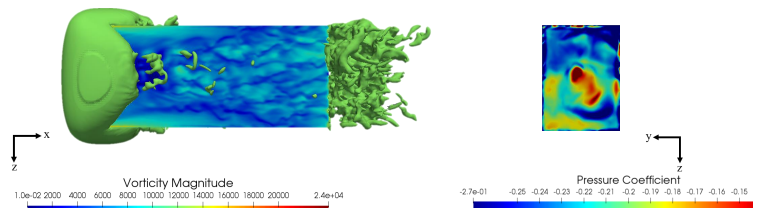

FIG. 11: Iso-contours of the coefficient of pressure $C_P = -0.2$ (left) and vorticity distribution on the body surface, indicating the effect of the feedback controller on the near wake vortical structures, with the associated C_p projected on the base (right).
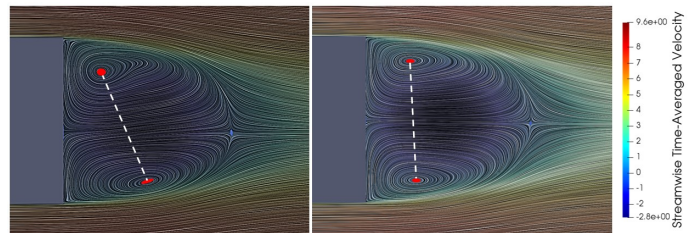

FIG. 12: Streamlines based on the time-averaged streamwise velocity projected on a plane at mid-height of the body. The unforced case is shown on the left and the controlled case ($B = 60$) is shown on the right.

associated with minimizing the imprint of the toroidal-vortex on the base, this being correlated with an increase in the average base pressure. For the present feedback control, the proximity of the toroidal-vortex to the base slightly hinders the recovery in average base pressure, which is likely to limit the reduction in pressure drag. The length of the recirculation region for the controlled case is reduced by 8% compared to the unforced case, with a value $\overline{L_{R-cont}} = 1.32H$. Thus the feedback control reduces the length of the recirculation bubble while also reducing the drag. This differs to findings in the absence of unsteady actuation or feedback control, where shorter recirculation bubbles imply increased drag [52, 53], but is consistent with other feedback control studies, where the change in the recirculation length was more related to actuation location than drag reduction [54]. Figure 12 shows the streamlines on a horizontal plane at the mid-height of the body. The unforced streamlines indicate the tilt of the toroidal vortex via a skewness of the vortex centers, while the controller restores the alignment of these centers, shortens the bubble length and increases the streamlines curvature.

C. Ahmed body drag

As mentioned in section §I, previous studies have suggested that a symmetric wake corresponds to $\sim 9\%$ base pressure recovery [16, 22]. This was estimated based
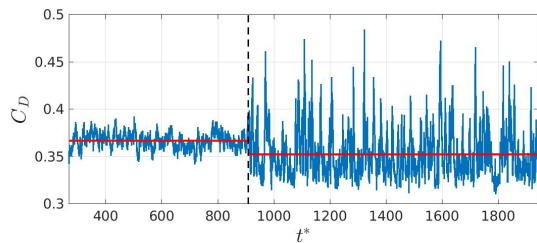
FIG. 13: Effect of feedback control on the drag coefficient (C_D). The controller is switched on at $t^* = 935$ shown with black dashed line. The values of the controller parameters A and B are 10 and 60, respectively. The red line indicates the mean values of C_D prior and after switching on the controller.

on comparing the average base pressure during switching events, when the wake is instantaneously symmetric, to its value while the wake is asymmetric. This suggests potential for reducing the pressure drag by suppressing wake bi-modality.

The current results confirm that resymmetrising the wake using nonlinear feedback control increases the average base pressure and reduces the pressure drag. The time-averaged drag is reduced with higher fluctuations of C_D, as shown in figure 13. $\overline{C_D}$ is reduced by 2.5% for the case with the controller parameters $A = 10$ and $B = 60$. Similar to mean flow properties, the percentage of drag reduction has a strong dependence on the value of B, that controls the contribution of the linear terms in the control low. This dependence leads to the parametric study in section §VII A. In case of $B = 1$, the time-averaged drag is reduced by 7.4%, which represents the maximum drag reduction achieved using the current nonlinear feedback controller. This reduction is lower than the expected 9%, due to the streamwise position of the toroidal vortex in the near wake. These simulations reveal that the drag reduction achieved by symmetrising the wake, depends on the way of suppressing wake bi-modality and its effect on the mean flow in the wake. To conclude, these results confirms that pressure drag is sensitive to wake bi-modality. The application of the nonlinear controller symmetrised the wake by affecting the separated shear layers in the separatix. This effect alters the balance of disturbances in shear layers and the streamwise position of the disturbances, which will be further discussed in section §VII C. The level of the disturbances imposed influences the base pressure and accordingly the drag.

D. Periodic modes in the wake

Here we investigate the effect of the controller on the time-periodic modes in the wake using spectral analysis of the base pressure. The symmetric and anti-symmetric base pressure signals considered in the following analysis are defined in equation 15 and 16, respectively, where M

is the number of the pressure probes, n_1 and n_2 are the distance of the pressure probes on the base to its center in either of the crossflow directions (y, z) as shown in figure 1.

$$\Delta P\big|_{\text{Symmetric}} = \frac{1}{M}\left[\sum_M P(x,y,z)\big|_{n_1} + \sum_M P(x,y,z)\big|_{n_2}\right] \tag{15}$$

$$\Delta P\big|_{\text{Anti-symmetric}} = \frac{1}{M}\left[\sum_M P(x,y,z)\big|_{n_1} - \sum_M P(x,y,z)\big|_{n_2}\right] \tag{16}$$

Figure 14 shows the effect of the controller on the anti-symmetric base pressure spectra in both the horizontal and vertical directions. The normalised frequency i.e. St number is calculated based on the body length in the direction of the anti-symmetric base pressure. The unforced signal in both directions indicates three periodic modes. The first appears with a broadband frequency around $St_W \sim 0.07$ in the horizontal signal (figure 14a) and around $St_H \sim 0.05$ in the vertical signal (figure 14b), is associated with the streamwise bubble pumping mode. This mode was detected in the base pressure spectrum in experiments by Khalighi *et al.* [55], and has been hypothesised to occur due to a periodic interaction of the top and bottom halves of the toroidal vortex trapped in the near wake region, causing a periodic change in the recirculation region. A further suggestion relates it to a non-linear interaction between the vertical and horizontal vortex shedding [20]. Although a linear stability analysis of the wake behind an axisymmetric body has not captured this mode [56], it has been detected in spectral analysis of the wakes of an axisymmetric body [5], a circular disc and a sphere wake [57]. The second mode is associated with a peak at $St_W = 0.19$ in the horizontal direction (figure 14a) and $St_H = 0.17$ in the vertical direction (figure 14b), and relates to vortex shedding in both directions. The same frequencies were reported in experimental studies by Volpe *et al.* [20] and Lahaye *et al.* [58]. The vortex shedding frequencies in both directions are consistent with the range of frequencies reported in the literature of $0.13 - 0.19$ [11, 29, 59]. The third dynamical mode, for the unforced base pressure, appears in figure 14 at $St_W \sim 1.9$ and $St_H \sim 1.6$ and is linked to the higher frequency dynamics of the shear layers in both directions.

The base pressure spectra, horizontally and vertically antisymmetric are shown in the presence of feedback control in figures 14a and 14b, respectively. Both signals capture the same periodic modes evidenced in absence of the controller. In the horizontal direction, the controller amplifies the energy content of all these modes. The horizontally anti-symmetric base pressure signal (figure 14a), captures the symmetric bubble pumping mode at the same frequency of the unforced case. Unlike for the unforced case, the controlled signal does not capture a
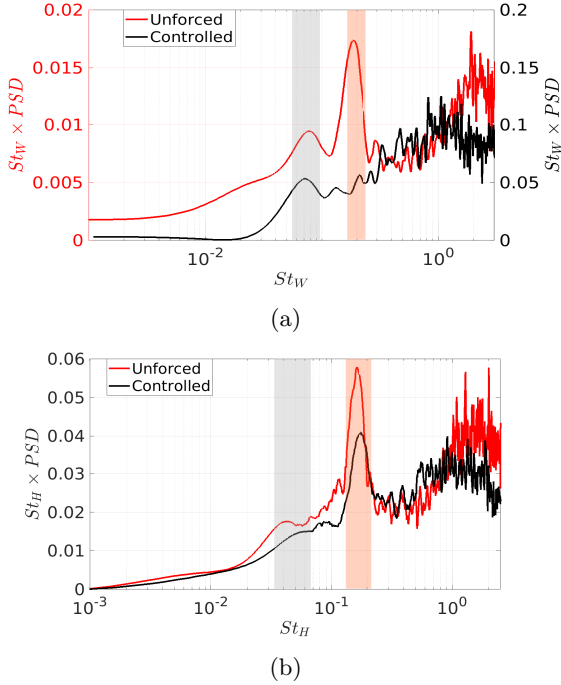
(a)

(b)

FIG. 14: Premultiplied spectra of the (a) horizontal and (b) vertical anti-symmetric base pressure signals for both the unforced (red) and the controlled (black) cases. Gray and red shaded areas indicate the broad frequency band related to the bubble pumping mode and vortex shedding frequency, respectively.
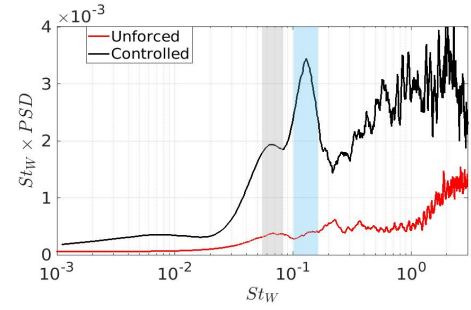

FIG. 15: Symmetric premultiplied base pressure signals for both unforced (red) and controlled (black) cases. Gray and blue shaded areas indicate the broad frequency band related to the bubble pumping mode and the frequency associated with the streamwise motion of the toroidal vortex, respectively.

clear peak for the horizontal vortex shedding. A relatively smaller peak around $St_W = 0.2$ is seen, this suggesting that the anti-phase low frequency forcing of the controller disturbs the dynamics of the horizontal vortex shedding. This will be further discussed using the POD analysis in section §VIII. The energy content of the free shear layers is increased by an order of magnitude in the presence of the feedback controller, with a relatively lower frequency of $St_W \sim 1$ compared to the unforced case ($St_W \sim 1.9$). Similarly, the vertically antisymmetric spectrum (figure 14b) shows how the controller slightly reduces the energy content of these three modes. The energy content of the vertical vortex shedding mode is reduced with a slight increase in the associated frequency from $St_H = 0.17$ without control to $St_H = 0.19$ with control. This shift in the vortex shedding frequency is consistent with the recent experimental results by Plumejeau et al. [23], which concluded that the symmetric wake configuration is associated with a higher shedding frequency in both cross-flow directions. The vertically anti-symmetric signal captures the shear layer dynamics at a frequency equivalent to $St_H \sim 1$, this frequency having shifted downwards compared to the uncontrolled case ($St_H \sim 1.6$).

The unforced symmetric base pressure signal, shown in figure 15, captures a broad frequency band around $St_W \sim 0.07$ related the bubble pumping and high fre-

quency shear layers dynamics at $St_W \sim 2.4$. The controller increases the energy content of the whole spectrum without changing the bubble pumping frequency. A clear frequency peak at $St_W \sim 1.3$ is evidenced in the presence of the feedback controller. This is attributed to a new symmetric behaviour linked to the effect of the momentum exchanged in the wake after control has been switched on. The new symmetric behaviour associated with frequencies of $St_W = 0.13$ ($St_H = 0.1$ in the vertical direction), is found to be related to streamwise motion of the near-wake toroidal vortex structure after it has symmetrised. Figure 16 shows the time evolution of the of the steamwise position of the toroidal-vortex represented by the pressure coefficient iso-surface. The time interval between each successive snapshot is equivalent to $St_W = 0.13$. In symmetrising the wake, the controller causing a transitional motion of this toroidal vortex. Dynamics of the shear layers are also captured in the controlled signal with an associated frequency of $St_W \sim 2$.

The effect of the controller on the dynamical modes in the wake can be concluded as follows; the low-frequency bubble pumping mode is largely unaffected by suppressing the horizontal bi-modal switching, and by the reduction in the high-frequency horizontal residual oscillations. The vertical vortex shedding frequency increases due to the action of control. The horizontal vortex shedding, however, has not been clearly evidenced, as the interaction of the horizontal shear layers is now disturbed by the controller. The different effects of the controller on the vortex shedding mode in the horizontal and vertical directions is attributed to the setup of the actuation slots, shown in figure 1. The horizontal shear layers are subjected to anti-phase forcing, while the vertical shear layers are forced in-phase. The stochastic horizontal switching of the wake is replaced by an oscillatory motion of the toroidal vortex structure in the streamwise direction, due to exchanging momentum between the lateral sides of the wake. Finally, the spectral analysis of the antisymmet-
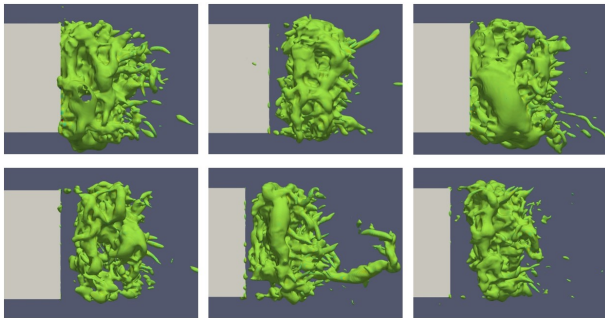
FIG. 16: Instantaneous snapshots of the near-wake toroidal-vortex indicated by the iso-contours of the pressure coefficient ($C_P = -0.2$). It indicates the time evolution of the streamwise location of the toroidal vortex with a time interval corresponding to $St_W = 0.13$ between each successive snapshots starting on the top-left to the bottom-right.

ric controlled signals indicates an increased energy level relative to the unforced case in the horizontal direction, while in the vertical direction the energy has decreased.

VII. NON-LINEARITY AND BI-MODALITY SUPPRESSION

As mentioned in Section VI, the performance of the feedback controller depends on the choice of controller parameters in the control law given by equation (12). A parametric study of the feedback control law parameters, A and B, is now carried out to investigate the effect on bi-modality suppression, drag and wake dynamics. Parameter A amplifies the control effort and directly affects the wake response time, resulting in a faster wake response for $A > 1$. The threshold value to symmetrise the wake is $A=10$, yet as A increases, the drag reduction decreases. This is likely to be because larger values of A increase the momentum coefficient and subsequently enhance the near wake entrainment. This directly affects the shear layers and their associated interactions, amplifying the higher frequency dynamics in the near wake region. Parameter B represents an amplification factor of the linear term of the control law. A range of $0 < B \leq 90$ is investigated for $A = 10$. Exploring the contribution of the linear term offers an insight into the effect of nonlinearity on suppressing bi-modality and its associated interactions in the wake. The effect of varying B is discussed in detail in the following subsections.

A. Wake symmetry, wake oscillations and body drag

The effect of varying B on the wake symmetry, residual oscillations, base pressure and drag reduction is firstly explored. The effect of varying B on the degree of wake-
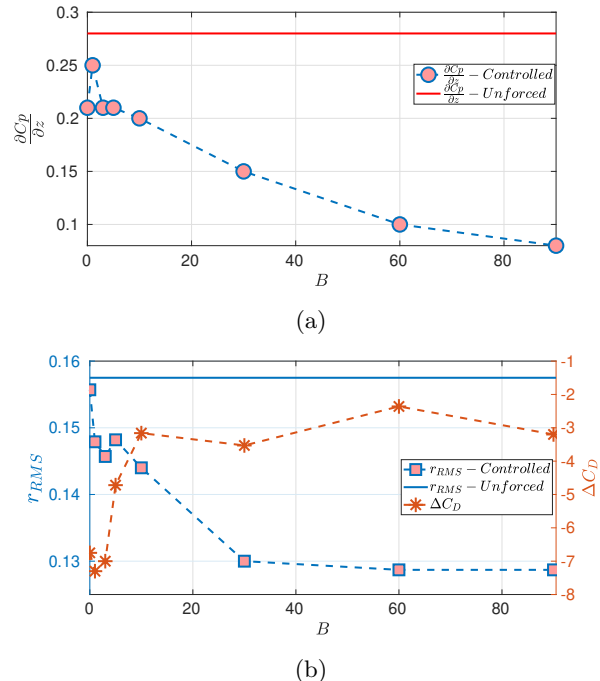

(a)

(b)

FIG. 17: (a) The variation of the horizontal gradient of the base pressure coefficient (used to indicate the level of wake-symmetry) with the controller parameter B. The red line indicates the value of $\partial C_p/\partial z$ for the unforced case. (b) Blue: Root Mean Square (RMS) of the instantaneous centre of pressure for different values of the amplifications factor, B. The blue solid line shows the RMS value for the uncontrolled case. Orange: the variation in drag reduction with B.

B	$\overline{C_{\text{Pbase}}}$	$\frac{\overline{L_R}}{H}$	$-\Delta\overline{C_D}\%$	$\overline{C_\mu} \times 10^3$	St_{control}
Unforced (Asymmetric wake)	-0.232	1.44	0.00	0.0	0
0.01	-0.209	1.36	6.75	1.2	0.021
1	-0.207	1.38	7.40	1.2	0.024
3	-0.208	1.37	7.00	1.2	0.025
5	-0.214	1.34	4.72	2.0	0.033
10	-0.217	1.33	3.16	3.0	0.034
30	-0.216	1.34	3.53	3.3	0.040
60	-0.218	1.32	2.50	3.9	0.054
90	-0.217	1.33	3.20	3.9	0.050

TABLE II: The effect of changing the amplification parameter B on the mean flow parameters; the time-averaged base pressure coefficient ($\overline{C_{\text{Pbase}}}$), the recirculation bubble length ($\overline{L_R}$), the average drag reduction ($\Delta\overline{C_D}$) and the control effort characterised by the momentum coefficient ($\overline{C_\mu}$) and the resultant frequency of the periodic switching in the wake (St_{control})

symmetry, which is characterised by the value of the horizontal gradient of the base pressure coefficient, $\partial C_p/\partial z$, is shown in figure 17a, with a more symmetric wake associated with lower values of $\partial C_p/\partial z$. It can be seen that the level of wake symmetry increases with B. For $0 < B < 10$, the same order of magnitude as the growth rate α, fluctuations in $\partial C_p/\partial z$ show a maximum reduction of 25% compared to the unforced case, and the wake exhibits little sensitivity to B. When B is one order of magnitude higher than α, i.e. $B > 10$, the wake symmetry starts to increase with B, the maximum reduction in wake asymmetry being reached at $B = 90$, beyond which no further reduction is achieved. The value of $\partial C_p/\partial z$ is then reduced by 72% compared to the unforced case and the wake can be considered symmetrised in this region. In this case (i.e. $B = 90$), the linear term dominates the control effort, with B almost two orders of magnitude higher than α. Relating the value of the linear term parameter, B, to the growth rate parameter, α, suggests that the growth of the mode r could be suppressed with a linear controller.

The residual wake oscillations around the mean wake position, characterised by the root mean square of r, r_{RMS}, are also affected by the tuning of B. As shown in figure 17b, r_{RMS} exhibits a decreasing trend as B increases, reaching a minimum when $B = 60$, without further reduction for higher values of B. This confirms a significant benefit of the present non-linear controller over the linear controllers employed in previous studies. There, control led to amplification of the horizontal residual oscillations, and this was linked to low values of drag reduction of less than $\sim 2\%$ [21, 34, 35]. Figure 17b also depicts the variation of the drag reduction as B varied. For the present results, low levels of horizontal residual oscillations do not seemed to be directly linked to drag reduction; when the residual oscillations are small, the mean drag reduction is also small. The maximum drag reduction achieved by feedback control is 7.4%, a significant increase on the 2% reported previously using a linear controller. For this maximum reduction, $B = 1$ (hence $0 < B \leq \alpha$), which means that the nonlinear term dominates the control effort, the wake then oscillates at a frequency of $St_{\text{control}} = 0.024$.

The drag reduction decreases as B increases and hence the contribution of the linear controller term increase. A minimum drag reduction of 2.5% occurs for a fully symmetrised wake, the residual fluctuations of the wake are also smallest. Comparing figures 17a and 17b, a trade-off between drag reduction and wake-symmetry is evident, suggesting that drag reduction is not directly related to symmetrising the wake, but linked to suppression of the nonlinear interactions between the stochastic bi-modality and other periodic modes in the wake. A favourable manipulation of these nonlinear interactions is attained when the nonlinear term of the controller dominates the control effort (i.e. $B \leq \alpha$), suggesting the need for a nonlinear controller in order to reduce the drag.

Table II shows the change in the mean flow properties

as B varies. The time-averaged base pressure coefficient, $\overline{C_{\text{Pbase}}}$, decreases with B, inhibiting the reduction in pressure drag. A linear relation between $\overline{C_{\text{Pbase}}}$ and $-\Delta\overline{C_D}\%$ can be seen here, confirming the dominant effect of the base pressure on pressure drag [4]. For all values of B, some base pressure recovery is evidenced compared to the unforced case. The maximum average increase in the base pressure was less than the 9% indicated in the literature. This is suggested to be a result of the controller shifting the near-wake toroidal vortex closer to the base, limiting the base pressure recovery. The minimum value of $\overline{C_{\text{Pbase}}}$ occurs for $B = 60$, and is associated with the least drag reduction. This case achieves a relatively high level of wake symmetry, with the linear control term dominating the control effort. The length of the recirculation bubble, $\overline{L_R}$, is reduced in presence of the feedback control for all values of B compared to the unforced case. This length also decreases as B increases. A reduction of 3.5% in $\overline{L_R}$ is reported for the case of maximum drag reduction ($B = 1$) compared to the asymmetric unforced wake, while a 9% reduction in $\overline{L_R}$ is reported for the minimum drag reduction. Comparing the controlled cases, it can be seen that a longer bubble allows for higher base pressure recovery and consequently reduced drag [21, 32]. However, we suggest that the underlying mechanism of drag reduction achieved here is not limited to the bubble length but is also influenced by the suppression of wake symmetry breaking.

B.   Control performance

The effect of tuning B can also be characterised using the barycenter of pressure, $r(\text{t})$, i.e. the controller input defined in equation (8). The maximum deviation of the wake from the center of the base in the absence of control corresponds to $r = \pm0.32$, which represents the switching bounds of the unforced wake. The contribution of the controller nonlinear term was assessed for different values of B. For $B = 0.01$, the controller is linear when the spatial position of the wake lies in the space $-0.05 \leq r \leq 0.05$. That is, the contribution of the nonlinear part of the controller is negligible when the wake is close to being symmetric. The contribution of the controller nonlinearity then increases as the wake deviates from the linearly dominated region. The range of r for which $u(r)$ is almost linear increases with B, implying a larger linearly dominated region for higher values of B. For $B = 90$, the linearly dominated region extends to $-0.14 \leq r \leq 0.14$, beyond which, the contribution of the nonlinear term in the control effort does not exceed 10%. This suggests the possibility of suppressing wake bi-modality using purely linear controllers, even though the nonlinearity inherent in the interactions of this mode with the other dynamical modes and the effect on drag reduction remain open questions.

Figure 18 shows the time history of the controller input, $r(t)$, and the output, $u(r)$. Both signals are peri-
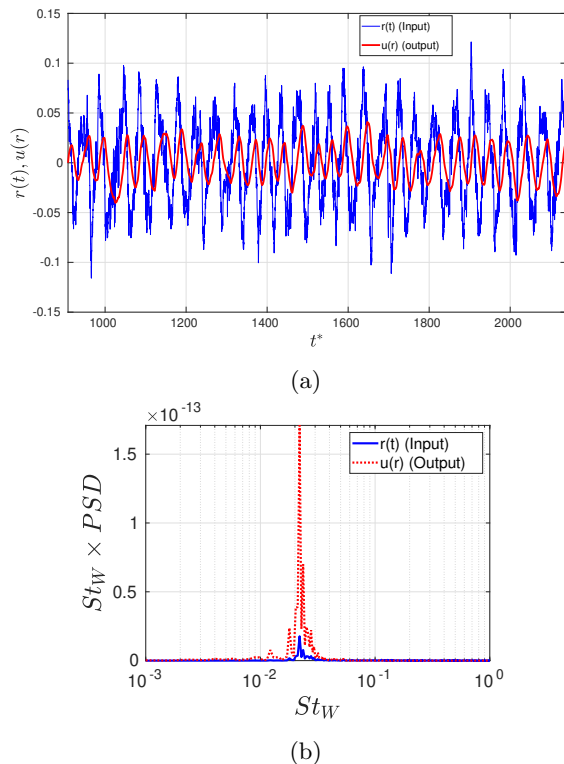
(a)

(b)

FIG. 18: (a) Time evolution of the input and output signals of the nonlinear controller for the case of $B = 1$. The associated frequency of both signals corresponds to $St_{\mathrm{control}} = 0.024$.
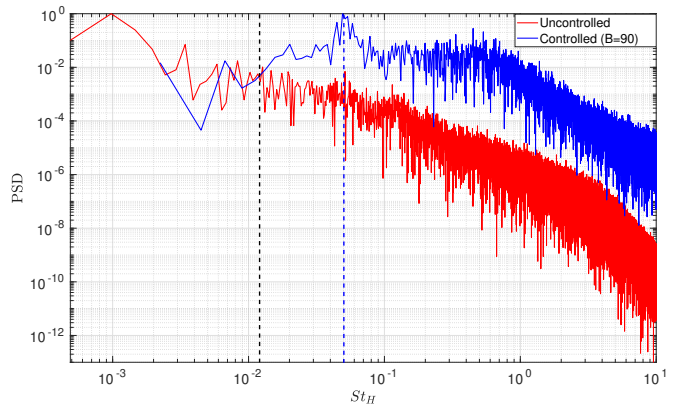

FIG. 19: Power Spectral Density (PSD) of the uncontrolled (red) and the controlled (blue) centre of pressure for the case of $B = 90$, indicating the cut-off frequency $St_{\mathrm{cut\text{-}off}} = 0.013$ (back dashed line) and the frequency peak for the controlled wake $St_{\mathrm{control}} = 0.05$ (blue dashed line).

odic with a frequency corresponding to $St_{\mathrm{control}} = 0.024$ for $B = 1$, the case where maximum drag reduction is achieved. The time delay between the signals is related to the wake response time to actuation. The value of St_{control}, which is associated with the wake oscillations that occur in the presence of feedback control, increases as B increases. For B in the range $0 < B \leq 90$, the frequency lies in the range $0.02 < St_{control} < 0.054$, as indicated in table II. The drag reduction decreases as St_{control} becomes closer to the bubble pumping frequency. The interaction between the periodic switching and the bubble pumping modes is seen to limit the drag reduction. Comparing the sensor signal, $r(t)$, for the controlled and uncontrolled cases, figure 19 indicates a cut-off frequency, $St_{cut\text{-}off}$, where the action of control starts to amplify rather than attenuate oscillations. Dynamical modes below $St_{cut\text{-}off}$ are attenuated, by the action of the control, while those above are amplified. Across different controller parameters, $St_{cut\text{-}off}$ has a similar order of magnitude to the peak bi-modality frequency, its value increasing as B increases, reaching a maximum value of $St_{cut\text{-}off} = 0.013$ for the case in which the linear control term exceeds the nonlinear term by two orders of magnitude and the wake is fully symmetrised ($B = 90$). Tighter switching bounds of the wake are associated with higher cut-off frequency. This indicates that the model con-

sidered here, based on Langevin dynamics, successfully captures the low frequency dynamics associated with bi-modality. If the synthetic jet actuators can be assumed to have an efficiency of $\eta_{\mathrm{actuator}} = 0.95$ (95%), the maximum power utilised by the controller, $Pw_{\mathrm{actuation}}$ would not exceed 0.5% of the total power saved due to drag reduction, Pw_{saved}.

The momentum coefficient of the actuation associated with control, C_μ, increases with B. The maximum C_μ for the case of maximum drag reduction ($B = 1$) was 8.5×10^{-3} with an average value of 1.2×10^{-3} (table II). As the momentum coefficient increases, the drag reduction decreases, reaching its minimum value when $C_\mu = 7.9 \times 10^{-2}$ with an average of 3.9×10^{-3}. This suggests that higher levels of momentum exchanged in the wake increase the level of turbulent entrainment in the near wake region, consistent with the description of flow dynamics in the wake by Gerrard [60]. Increasing C_μ enhances the unsteadiness of the streamwise momentum, which has an unfavourable effect on the drag. The higher levels of momentum exchanged in the wake further increase the disturbances on the free shear layers that have been balanced due to wake reorientation, as discussed previously, which hinders the gain in drag reduction. This suggests that a new control strategy which attenuates the disturbances in the free shear layers might be more effective for reducing the drag.

C. Insights into bi-modal switching mechanism

The results suggest that bi-modality indirectly affects the drag through the interaction of the asymmetric recirculation region and the shear layers that are shed from the vertical base edges between which switching takes
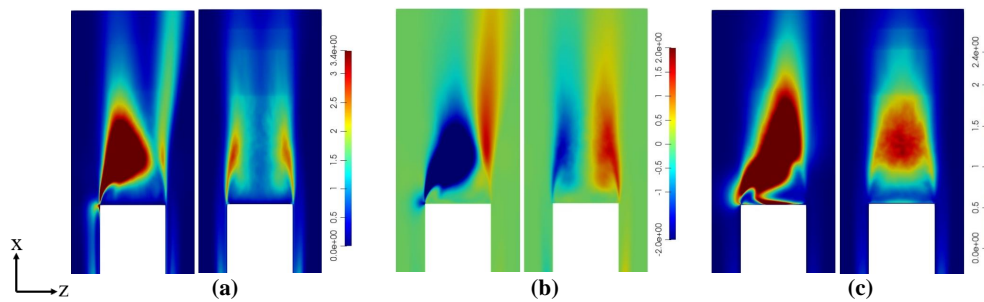
FIG. 20: Time-averaged Reynolds stress components on a central horizontal plane at $y/H = 0.5$. Comparing the uncontrolled asymmetric wake (on the left for each component) and the controlled case (on the right for each component). (a) The streamwise Reynolds stress $\overline{u'_x u'_x}$. (b) The $\overline{u'_x u'_z}$ Reynolds stress. (c) The horizontal (lateral) Reynolds stress $\overline{u'_z u'_z}$.
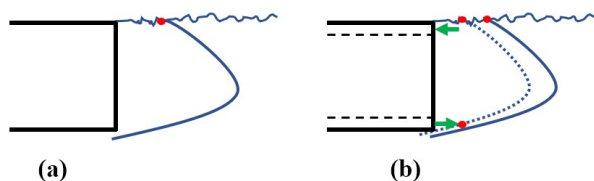

FIG. 21: Schematic description of the effect of the controller on the shear layers in the switching direction. The asymmetric recirculation region formed by the bottom shear layer and its triggering to the top shear layer in the unforced case is shown in (a). The effect of momentum exchange on both shear layers is indicated in (b), where the continuous and dashed lines represent the unforced and the controlled recirculation regions respectively.

place. Haffner *et al.* [22] recently proposed a mechanism for the wake switching based on flow entrainment related to the lateral shear layer dynamics. Their experimental results suggest that the formation of an asymmetric recirculation region is caused by the large curvature of one shear layer. This curved shear layer triggers the parallel layer downstream of the base, causing a roll-up in the wake which leads to a shedding of a hairpin vortex in the wake [18]. This roll-up creates an engulfed flow that increases the flow entrained into the recirculation region. As this roll-up gets stronger, the triggered shear layer starts to curve forming a new recirculation region opposite to the existing one, leading to a transient symmetric wake. This mechanism is consistent with the present simulations, as shown through the projected streamlines based on the streamwise velocity during the switching event included in the supplementary movie. The drag reduction associated with this transient symmetric wake is related to inhibiting both the trigger of the shear layers and the coherent recirculating motion in the near wake region [22]. The trigger of the shear layers can be indicated by Reynolds stresses in the wake.

Figure 20 compares the Reynolds stresses on a hori-zontal plane at the mid-height of the body for the asymmetric unforced wake and the controlled wake. An asymmetric pattern is indicated in all three components ($\overline{u'_x u'_x}$, $\overline{u'_x u'_z}$, $\overline{u'_z u'_z}$) for the unforced case. The triggering of the shear layer on the right side of the body ($+z$ direction) is indicated by relatively higher stresses in the stream-wise direction ($\overline{u'_x u'_x}$) downstream of the base, while the curved shear layers forming the asymmetric recircula-tion region exhibit higher levels of both the $\overline{u'_x u'_x}$ and $\overline{u'_x u'_z}$ shear stress components. The spanwise component ($\overline{u'_z u'_z}$) has higher levels towards the triggered shear layer side. For the controlled symmetric wake, the wake ex-hibits balanced shear stresses on both shear layers.

In the presence of the controller, exchanged momentum through the actuation slots imposes direct disturbances on both shear layers at the separation edges. These disturbances disrupt the switching mechanism discussed above. When the wake resides on one side, the actuation starts to blow air, introducing disturbances on the curved shear layer, while the parallel triggered layer is now sub-jected to suction by the actuator slot, i.e. shifting the triggering location upstream towards the base and in-creasing its curvature. The application of the controller with anti-phase forcing – blowing on the large curved shear layer and suction on the triggered layer – will have the following effect (figure 21):

- The blowing on the curved shear layer increases the curvature of this shear layer and accordingly reduces the length of the recirculation region.

- This effect forces the triggering location of the par-allel layer to take place further upstream, closer to the base.

- Applying suction on the other side will have two effects; imposing disturbances on this shear layer closer to the base, promoting earlier growth and promoting the formation of the opposite recircula-tion region.

- When the level of momentum exchanged between the lateral sides and the wake increases, this sig-

nificantly amplifies the balanced disturbances on the shear layers and accordingly decreases the base pressure (table II).

Although the application of the controller here inhibits the coherent recirculation in the near-wake, which has a favourable effect for drag reduction similar to the symmetric transient state of the unforced case, the disturbances imposed on both shear layers limits the gain in drag reduction. The shear layers disturbances are now balanced, and shifted upstream closer to the base, yielding a more pronounced effect on the base pressure and limiting the drag reduction. The maximum gain in drag reduction is achieved for the case where minimum shear layer disturbances are imposed due to the exchanged momentum. The imposed disturbances on the shear layers amplifies the higher frequency dynamics in the near wake region, which is confirmed by comparing the power spectral density of r in the absence and presence of control, shown in figure 19. Although bi-modality is a random behaviour of the wake, the unforced flow exhibits a broad peak at $St_H \sim 10^{-3}$. The effect of control is to amplify the higher wake frequencies, which are associated with $St_H > St_{\text{cut-off}}$. We speculate that this amplification creates a coupling between bi-modality and the low frequency bubble pumping mode, consequently driving the random dynamics of bi-modality into regular oscillations of the toroidal-vortex within spatial bounds closer to the centre. This can be evidenced by the match between the frequency range of the wake oscillations and the bubble pumping frequency. This coupling further causes streamwise oscillations of the toroidal-vortex, similar in behaviour to the bubble pumping at a frequency of $St_H = 0.1$, as indicated in section VI D. Thus, the controller changes the stochastic switching of the toroidal-vortex into spatially-bounded oscillatory switching with streamwise oscillations of this vortex. To conclude, drag reduction is found to be related to the effect of bi-modality on the shear layers in the switching direction. Bi-modality suppression balances the disturbances in the two parallel shear layers and shifts the streamwise position of the shear layers triggers upstream closer to the base, which found to be unfavorable for base pressure recovery.

VIII. PROPER ORTHOGONAL DECOMPOSITION

In order to obtain more insights into the effect of control on bi-modality suppression, Proper Orthogonal Decomposition (POD [61]) of the pressure data on a horizontal plane - parallel to the ground - at mid-height of the body, is now considered. The total acquisition time was 1000 convective time units, which was deemed sufficient for statistical convergence. The wake residence time within each asymmetric position was equal to that for the unforced case. The sampling frequency corresponded to $St_W = 2.84$, with $St_W = fW/U_\infty$, where f
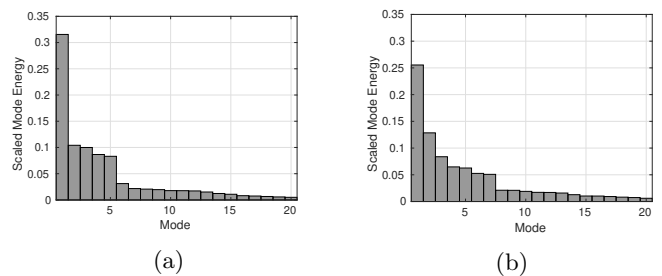

FIG. 22: Energy content of the first 20 pressure POD modes for the unforced (a) and the controlled case for $B = 60$ (b).
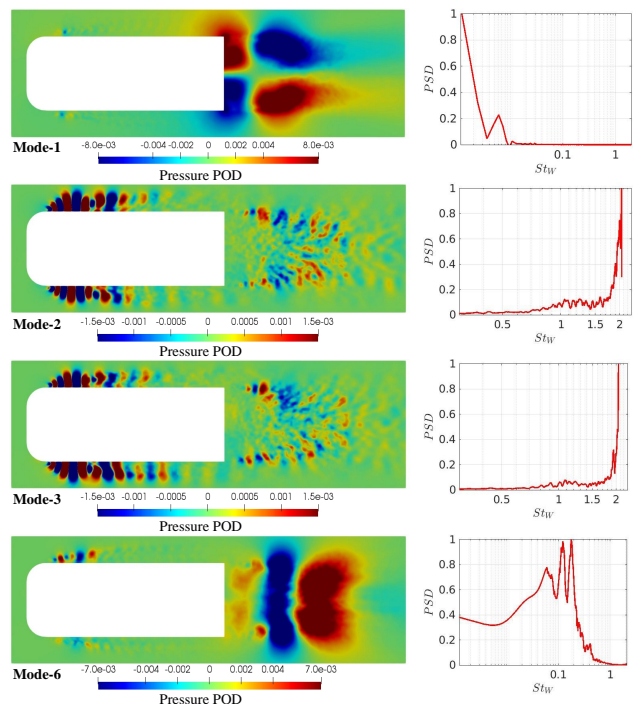

FIG. 23: Pressure POD on a horizontal mid-plane for the unforced case (left) and their associated power spectral density of their coefficients (right).

is the frequency in Hz. This sampling frequency resolves the highest frequency in the wake.

A. Unforced POD

The energy content of the first twenty modes is shown in figure 22a. The most energetic first six modes contain $\sim 73\%$ of the total energy. Reflectional Symmetry Breaking *(RSB)* mode, represented by mode-1 in figure 23, is the most energetic, with an energy content of 32%, similar to the experimental results by Schmidt *et al.* [35]. This mode is antisymmetric and captures the dynamics of the toroidal vortex structure in the near-wake region, consistent with the recent DNS results by Podvin *et al.*

[31]. Spectral analysis of the time coefficient of this mode indicates a broad energy peak at very low frequencies of an order of $St_W \sim 0.001$. The next four modes capture the dynamics of the frontal separation bubble and the free shear layers in the wake, containing $\sim 37\%$ of the POD total energy. These modes are associated with the separation and the reattachment of the turbulent boundary layers on the side surfaces of the body. A causal link between the frontal separation bubble dynamics and bimodality was recently suggested by Hesse and Morgans [30]. The power spectral densities of the POD coefficients exhibit peaks at $St_W \approx 1 \sim 2$. The higher frequency $St_W \sim 2$ is linked to the frontal separation bubble, as it matches the dominant frequency of the pressure signal at the bubble location. The broadband dynamics around $St_W \sim 1$ are related to shear layer roll-up in the wake, which is suggested to be related to the switching mechanism [22]. Mode-2 and mode-4 have similar structures with a shift in space denoting the convective nature of these modes; the same is true for mode-3 and mode-5. Both mode-4 and mode-5 are not shown for brevity.

Mode-6 in figure 23 further shows a mode of combined vortex shedding and bubble pumping. Spectral analysis of the modes' temporal coefficient indicates three peaks at $St_W = 0.06$, $St_W = 0.15$ and $St_W = 0.17$, the first frequency indicating the bubble pumping and the last two associated with the vortex shedding. The time evolution of this combined mode indicates that the energy level varies between the two sides of the wake, depending on the side of the vortex shedding, associated with the asymmetric position of the wake. These results match the POD analysis of the Ahmed body wake using direct numerical simulation by Podvin *et al.* [31].

B. Controlled POD

The effect of the controller ($B = 60$ case) on the horizontal POD modes is shown in figure 24. Similar to the unforced case, the RSB mode, represented by mode-1 in figure 24, remains as the most energetic mode, although, its energy content is reduced by 10% compared to the unforced case (figure 22b). It is associated with a frequency of $St_W = 0.054$, indicating the effect of the controller in replacing the stochastic switching with periodic oscillations. Figure 24 shows that the second POD mode is symmetric and dominated by the streamwise oscillation of the torioidal vortex at a frequency of $St_W = 0.13$, which was captured previously by the base pressure signal (figure 14a) and the time-resolved wake topology (figure 16). This mode contains 13% of the total energy of the flow and further captures the dynamics of the bubble pumping associated with $St_W \sim 0.06$ and the shear layer roll-ups at $St_W \sim 0.5$. Similarly, the third POD mode is symmetric and captures both the streamwise oscillations of the toroidal vortex and the shear layer dynamics represented as a symmetric shedding, and it is not shown for brevity.
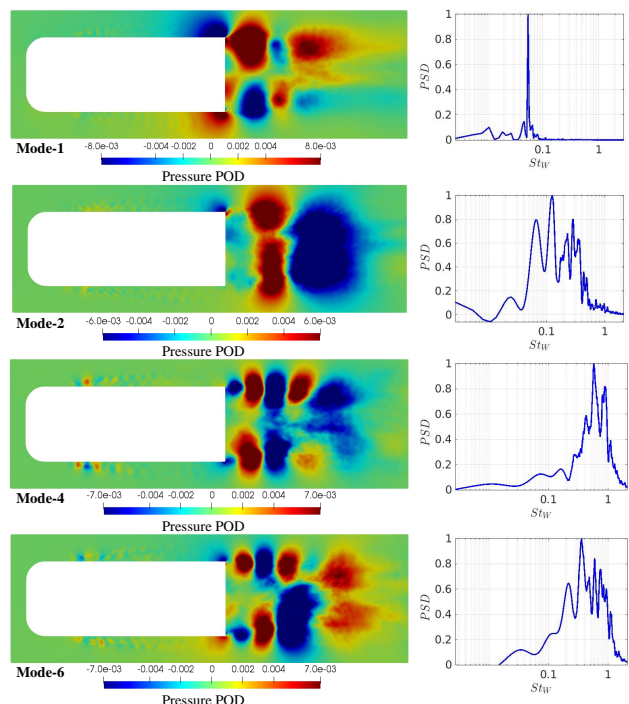

FIG. 24: Pressure POD on a horizontal mid-plane (left) and the associated power spectral density of their coefficients (right) for the controlled case ($B = 60$).

Figure 24 shows the fourth mode, which indicates a symmetric shedding of the free shear layers in the wake at a frequency of $St_W \sim 0.5$. These dynamics were captured by Haffner *et al.* [22], and were suggested to be subharmonics of the shear layer roll-ups occurring downstream of the base (at $x/H \approx 0.3$ from the base) in the unforced case. However, in the presence of the controller, the anti-phase forcing exchanges momentum between the lateral sides of the wake, shifting these dynamics upstream closer to the base. Compared to the unforced case, the shedding of each shear layer in the controlled case is partially attributed to the actuation, while in the unforced case it was triggered by the interaction with the parallel shear layer. The horizontal vortex shedding is evidenced in anti-symmetric mode-6 at $St_W \sim 0.22$. The energy content of the vortex shedding is doubled compared to the unforced flow. Mode-5 and mode-7 have the same patterns and frequencies as mode-4 and mode-6, respectively, hence are not shown.

The effect of the non-linear feedback controller on the pressure POD can then be summarised as follows; the energy content of the static RSB mode is reduced and the stochastic switching of the wake is changed to periodic oscillations accompanied by streamwise oscillations of the near-wake toroidal vortex. The energy content of both the horizontal (spanwise) vortex shedding and the free shear layer dynamics are intensified by exchanging momentum in the wake. The increase in the energy level of these modes is expected to limit the drag reduction achieved by wake symmetrisation. This increase in the

energy content, which is associated with the symmetrisation of the toroidal vortex structure, is consistent with the DNS results of Podvin *et al.* [31].

The current controller, despite forcing the locked-in toroidal vortex in the near wake region, is seen to also significantly affect the separated shear layers affecting other periodic modes in the wake. This confirms the complexity of the interaction between the bi-modality and other dynamical modes of the flow. To conclude, the interaction between the wake and the side shear layers can be viewed as an external forcing on the shear layers. This is consistent with the recent experimental study by Haffner *et al.* [22] on the mechanism of bi-modality inline with the previous study by Gerrard [60] on the mechanism of formation of the recirculation region and its relation the entrainment caused by the shear layers in the wake of 2D bodies.

IX. CONCLUSION

The turbulent wake behind a squareback Ahmed body has been investigated using high fidelity wall-resolved large eddy simulations. The simulations successfully captured stochastic bi-modal switching from side-to-side as well as three time-periodic modes in the wake: vortex shedding in both cross-flow directions, roll-up of the free shear layers and a streamwise pumping motion of the recirculation bubble. The latter showed a distinguishable mark on the base pressure, which has not been detected in most previous experimental studies. Bi-modality was found to be the most energetic dynamical mode in the wake.

Wake bi-modal switching has previously been suppressed with linear control but resulted in large amplitude oscillations of the wake around the center. This study represents a first attempt to employ a nonlinear model-based controller to suppress the bi-modal switching. Bi-modality is modelled using Langevin dynamics. The controller, derived using a quadratic Lyapunov function, successfully suppresses the bi-modal switching. Furthermore, the resulting levels of wake fluctuations are significantly lower than for previous linear controllers. The extent of the fluctuations in asymmetry is significantly reduced. The nonlinear term of the controller is significant when the asymmetric positions of the wake deviates away from the linearly dominated region. The action of control changes the stochastic horizontal switching of the wake to an oscillatory motion of the large coherent structure in the near wake region, with frequency close to the bubble pumping frequency. The controller does not affect the bubble pumping frequency in the wake, yet leads to stronger and more energetic vortex shedding in both the horizontal and vertical directions.

Changing the relative contributions of the linear and nonlinear terms in the control law significantly changes the wake response. The general trend of driving the stochastic bi-modality to time-periodic oscillations holds in all cases, with a trade-off between drag reduction and level of wake asymmetry. A maximum drag reduction of 7.4% is achieved for a semi-symmetrised wake, for which the wake switches periodically between asymmetric positions. A fully symmetrised wake with a minimum in residual oscillations around the center of the base corresponds to 2.5% reduction in the drag. Suppressing the wake bi-modality using feedback control was shown to re-orient the toroidal vortex structure in the near wake region so that it becomes parallel to the base as well as closer to the base. This consequently disturbs the near-wake shear layers close to the base, limiting the base pressure recovery. It is proposed that this is the main reason that drag reduction is hindered in the case of a full-symmetrised wake. An indirect link between bi-modality suppression and drag reduction is shown. Drag reduction is found to be more sensitive to the interaction between the wake bi-modal behaviour and the shear layers in the switching direction. The effect of this interaction on drag depends on two effects: the unbalanced disturbances imposed on the shear layers and the streamwise position of the disturbances. The latter has a pronounced effect on the base pressure and hence the pressure drag. Controlling this interaction may offer more significant drag reductions, similar to those previously achieved using a base-cavity. The current results suggest that control strategies should focus more on suppressing or delaying the interaction between the separated shear layers and the coherent structures in the near-wake region to reduce drag. It also suggests that the actuation position is crucial for suppressing bi-modality without amplifying the disturbance on these shear layers.

[1] M. N. Sudin, M. A. Abdullah, S. A. Shamsuddin, F. R. Ramli, and M. M. Tahir, Review of research on vehicles aerodynamic drag reduction methods, Int. J. Mech. Mechatron. Engng **14**, 37 (2014).

[2] A. Seifert, O. Stalnov, D. Sperber, G. Arwatz, V. Palei, S. David, I. Dayan, and I. Fono, Large trucks drag reduction using active flow control, in *The Aerodynamics of Heavy Vehicles II: Trucks, Buses, and Trains* (Springer, 2009) pp. 115–133.

[3] W.-H. Hucho, ed., *Aerodynamics of Road Vehicles* (Butterworth-Heinemann, 1987).

[4] S. R. Ahmed, G. Ramm, and G. Faltin, Some salient

features of the time-averaged ground vehicle wake, SAE Transactions , 473 (1984).

[5] G. Rigas, A. R. Oxlade, A. S. Morgans, and J. F. Morrison, Low-dimensional dynamics of a turbulent axisymmetric wake, J. Fluid Mech. **755** (2014).

[6] M. Grandemange, M. Gohlke, and O. Cadot, Statistical axisymmetry of the turbulent sphere wake, Exp. Fluids **55**, 1 (2014).

[7] E. G. Duell and A. R. George, Experimental study of a ground vehicle body unsteady near wake, SAE transactions , 1589 (1999).

[8] S. Krajnovic and L. Davidson, Numerical study of the flow around a bus-shaped body, J. Fluids Engng **125**, 500 (2003).

[9] P. W. Bearman, Near wake flows behind two-and three-dimensional bluff bodies, J. Wind Engng Ind. Aerodyn. **69**, 33 (1997).

[10] W. T. Mason and P. S. Beebe, The drag related flow field characteristics of trucks and buses, in *Aerodynamic Drag Mechanisms of Bluff Bodies and Road Vehicles* (Springer, 1978) pp. 45–93.

[11] M. Grandemange, M. Gohlke, and O. Cadot, Turbulent wake past a three-dimensional blunt body. Part 1. Global modes and bi-stability, J. Fluid Mech. **722**, 51 (2013).

[12] M. Grandemange, O. Cadot, and M. Gohlke, Reflectional symmetry breaking of the separated flow over three-dimensional bluff bodies, Phys. Rev. E **86**, 035302 (2012).

[13] G. Bouchet, M. Mebarek, and J. Dušek, Hydrodynamic forces acting on a rigid fixed sphere in early transitional regimes, Eur. J. Mech. **25**, 321 (2006).

[14] O. Evstafyeva, A. S. Morgans, and L. Dalla Longa, Simulation and feedback control of the Ahmed body flow exhibiting symmetry breaking behaviour, J. Fluid Mech. **817** (2017).

[15] G. Rigas, A. S. Morgans, R. D. Brackston, and J. F. Morrison, Diffusive dynamics and stochastic models of turbulent axisymmetric wakes, J. Fluid Mech. **778** (2015).

[16] M. Grandemange, M. Gohlke, and O. Cadot, Bi-stability in the turbulent wake past parallelepiped bodies with various aspect ratios and wall effects, Phys. Fluids **25**, 095103 (2013).

[17] A. Kourta and C. Leclerc, Characterization of synthetic jet actuation with application to Ahmed body wake, Sens. Actuators A Phys. **192**, 13 (2013).

[18] L. Dalla Longa, O. Evstafyeva, and A. S. Morgans, Simulations of the bi-modal wake past three-dimensional blunt bluff bodies, J. Fluid Mech. **866**, 791 (2019).

[19] O. Cadot, A. Evrard, and L. Pastur, Imperfect supercritical bifurcation in a three-dimensional turbulent wake, Phys. Rev. E **91**, 063005 (2015).

[20] R. Volpe, P. Devinant, and A. Kourta, Experimental characterization of the unsteady natural wake of the full-scale square back Ahmed body: flow bi-stability and spectral analysis, Exp. Fluids **56**, 99 (2015).

[21] R. D. Brackston, J. M. García De La Cruz, A. Wynn, G. Rigas, and J. F. Morrison, Stochastic modelling and feedback control of bistability in a turbulent bluff body wake, J. Fluid Mech. **802**, 726 (2016).

[22] Y. Haffner, J. Borée, A. Spohn, and T. Castelain, Mechanics of bluff body drag reduction during transient near-wake reversals, J. Fluid Mech **894** (2020).

[23] B. Plumejeau, L. Keirsbulck, S. Delprat, M. Lippert, and W. Abassi, Behavior of the square-back Ahmed body global modes at low ground clearance, Phys. Rev. Fluids

5, 084701 (2020).

[24] D. Barros, J. Borée, O. Cadot, A. Spohn, and B. R. Noack, Forcing symmetry exchanges and flow reversals in turbulent wakes, J. Fluid Mech. **829** (2017).

[25] A. N. Rao, G. Minelli, J. Zhang, B. Basara, and S. Krajnović, Investigation of the near-wake flow topology of a simplified heavy vehicle using PANS simulations, J. Wind Engng Ind. Aerodyn. **183**, 243 (2018).

[26] R. Verzicco, M. Fatica, G. Iaccarino, P. Moin, and B. Khalighi, Large eddy simulation of a road vehicle with drag-reduction devices, AIAA J. **40**, 2447 (2002).

[27] E. Serre, M. Minguez, R. Pasquetti, E. Guilmineau, G. B. Deng, M. Kornhaas, M. Schäfer, J. Fröhlich, C. Hinterberger, and W. Rodi, On simulating the turbulent flow around the Ahmed body: A French–German collaborative evaluation of LES and DES, Comput. Fluids **78**, 10 (2013).

[28] R. Pasquetti and N. Peres, A penalty model of synthetic micro-jet actuator with application to the control of wake flows, Comput. Fluids **114**, 203 (2015).

[29] J.-M. Lucas, O. Cadot, V. Herbert, S. Parpais, and J. Délery, A numerical investigation of the asymmetric wake mode of a squareback Ahmed body–effect of a base cavity, J. Fluid Mech. **831**, 675 (2017).

[30] F. Hesse and A. S. Morgans, Simulation of wake bimodality behind squareback bluff-bodies using LES, Comput. Fluids , 104901 (2021).

[31] B. Podvin, S. Pellerin, Y. Fraigneau, A. Evrard, and O. Cadot, Proper Orthogonal Decomposition Analysis and Modelling of the wake deviation behind a squareback Ahmed body, Phys. Rev. Fluids **5**, 064612 (2020).

[32] A. Evrard, O. Cadot, V. Herbert, D. Ricot, R. Vigneron, and J. Délery, Fluid force and symmetry breaking modes of a 3D bluff body with a base cavity, J. Fluids and Struct. **61**, 99 (2016).

[33] M. Grandemange, M. Gohlke, and O. Cadot, Turbulent wake past a three-dimensional blunt body. Part 2. Experimental sensitivity analysis, J. Fluid Mech. **752**, 439 (2014).

[34] R. Li, D. Barros, J. Borée, O. Cadot, B. R. Noack, and L. Cordier, Feedback control of bimodal wake dynamics, Exp. Fluids **57**, 158 (2016).

[35] H.-J. Schmidt, R. Woszidlo, C. N. Nayeri, and C. O. Paschereit, The effect of flow control on the wake dynamics of a rectangular bluff body in ground proximity, Exp. Fluids **59**, 107 (2018).

[36] R. Manceau, Report on the 10th joint ERCOFTAC (SIG-15)/IAHR/QNET-CFD Workshop on Refined Turbulence Modelling, Poitiers, october 10-11, 2002, ERCOFTAC Bulletin **57**, 11 (2003).

[37] S. Jakirlic, R. Jester-Zürker, and C. Tropea, 9th ERCOFTAC/IAHR, in *COST workshop on refined turbulence modelling* (2001) pp. 36–43.

[38] TheOpenFOAMFoundation, OpenFOAM v6 User Guide, https://cfd.direct/openfoam/user-guide-v6 (2018).

[39] F. Nicoud and F. Ducros, Subgrid-scale stress modelling based on the square of the velocity gradient tensor, Flow Turbul. Combust. **62**, 183 (1999).

[40] U. Piomelli and J. R. Chasnov, Large-eddy simulations: theory and applications, in *Turbulence and transition modelling* (Springer, 1996) pp. 269–336.

[41] Y. Fan, C. Xia, S. Chu, Z. Yang, and O. Cadot, Experimental and numerical analysis of the bi-stable turbulent wake of a rectangular flat-backed bluff body, Physics of

Fluids **32**, 105111 (2020).

[42] R. J. A. Howard and M. J. B. M. Pourquie, Large eddy simulation of an Ahmed reference model, J. Turbul. **3**, 012 (2002).

[43] B. F. W. Gschaider, README for swak4Foam - Version for OpenFOAM 2.x, `https://github.com/Unofficial-Extend-Project-Mirror/openfoam-extend-swak4Foam-dev/blob/master/README` (2020).

[44] Y. Eulalie, P. Gilotte, I. Mortazavi, and P. Bobillier, Wake analysis and drag reduction for a square back Ahmed body using LES computations, in *ASME 2014 4th Joint US-European Fluids Engineering Division Summer Meeting collocated with the ASME 2014 12th International Conference on Nanochannels, Microchannels, and Minichannels* (American Society of Mechanical Engineers Digital Collection, 2014).

[45] B. Khalighi, K. Chen, and G. Iaccarino, Unsteady aerodynamic flow investigation around a simplified square-back road vehicle with drag reduction devices, J. Fluids Engng **134** (2012).

[46] M. Rouméas, P. Gilliéron, and A. Kourta, Analysis and control of the near-wake flow over a square-back geometry, Comput. Fluids **38**, 60 (2009).

[47] M. Minguez, R. Pasquetti, and E. Serre, High-order large-eddy simulation of flow over the "Ahmed body" car model, Phys. Fluids **20**, 095101 (2008).

[48] Z. Artstein, Stabilization with relaxed controls, Nonlinear Anal. Theory Methods Appl. **7**, 1163 (1983).

[49] L. Wong, F. H. Leung, and P. K. Tam, Lyapunov-function-based design of fuzzy logic controllers and its application on combining controllers, IEEE Trans. Ind. Electron. **45**, 502 (1998).

[50] L. Dalla Longa, A. S. Morgans, and J. A. Dahan, Reducing the pressure drag of a D-shaped bluff body using linear feedback control, Theor. Comput. Fluid Dyn. **31**, 567 (2017).

[51] E. Varon, J. Aider, Y. Eulalie, S. Edwige, and P. Gilotte, Adaptive control of the dynamics of a fully turbulent bimodal wake using real-time PIV, Exp. Fluids **60**, 1 (2019).

[52] M. Lorite-Díez, J. Jiménez-González, L. Pastur, C. Martínez-Bazán, and O. Cadot, Experimental analysis of the effect of local base blowing on three-dimensional wake modes, J. Fluid Mech. **883** (2020).

[53] E.-C. Hsu, L. Pastur, O. Cadot, and V. Parezanović, A fundamental link between steady asymmetry and separation length in the wake of a 3d square-back body, Experiments in Fluids **62**, 1 (2021).

[54] J. A. Dahan, A. Morgans, and S. Lardeau, Feedback control for form-drag reduction on a bluff body with a blunt trailing edge, Journal of Fluid Mechanics **704**, 360 (2012).

[55] B. Khalighi, S. Zhang, C. Koromilas, S. Balkanyi, L. P. Bernal, G. Iaccarino, and P. Moin, Experimental and computational study of unsteady wake flow behind a bluff body with a drag reduction device, SAE transactions , 1209 (2001).

[56] G. Rigas, L. Esclapez, and L. Magri, Symmetry breaking in a 3D bluff-body wake, arXiv preprint arXiv:1703.07405 (2017).

[57] E. Berger, D. Scholz, and M. Schumm, Coherent vortex structures in the wake of a sphere and a circular disk at rest and under forced vibrations, Journal of Fluids and Structures **4**, 231 (1990).

[58] A. Lahaye, A. Leroy, and A. Kourta, Aerodynamic characterisation of a square back bluff body flow, Int. J. Aerodyn. **4**, 43 (2014).

[59] N. Kang, E. E. Essel, V. Roussinova, and R. Balachandar, Effects of approach flow conditions on the unsteady three-dimensional wake structure of a square-back Ahmed body, Phys. Rev. Fluids **6**, 034613 (2021).

[60] J. H. Gerrard, The mechanics of the formation region of vortices behind bluff bodies, J. Fluid Mech. **25**, 401 (1966).

[61] L. Sirovich, Turbulence and the dynamics of coherent structures. I. Coherent structures, Q. Appl. Math. **45**, 561 (1987).